QUIETDRONES 2024
MANCHESTER
8th - 11th September 2024

Efficient prediction of propeller noise at incidence

Session: UAS/UAM Noise Prediction

Furkat Yunus, Delft University of Technology, The Netherlands,
f.yunus@tudelft.nl
Damiano Casalino, Dassault Systemes Deutschland GmbH, Germany,
damiano.casalino@3ds.com
Gianluca Romani, Dassault Systemes Deutschland GmbH, Germany,
gianluca.romani@3ds.com
Mirjam Snellen, Delft University of Technology, The Netherlands,
m.snellen@tudelft.nl

Abstract This paper investigates the prediction accuracy and time efficiency of two distinct low-order methods, *Opty∂B* and LOPNOR, for predicting tonal and broadband noise of a drone rotor in axial and non-axial flow conditions. These are both derived from an aerodynamic rotor model based on the blade element momentum theory, respectively coupled with a time- (*Opty∂B*) and frequency-domain (LOPNOR) solution of the Ffowcs Williams-Hawkings (FW-H) integral equation applied to a radial distribution of acoustically compact and non-compact sources. Experimental data and scale-resolving lattice-Boltzmann/very-large eddy simulation (LB/VLES) results for a two-bladed small unmanned aerial system (sUAS) in transitional boundary layer conditions are used to validate the low-order approaches. Comparison between low-order, high-fidelity and experimental results reveal that the underlying sound generation mechanisms are accurately modelled by the low-fidelity methods, which therefore constitute a valid tool for preliminary design of quiet drone rotors or to estimate the noise impact of drone operations.

Nomenclature

α	airfoil angle of attack	ψ	azimuthal angle
α_P	propeller angle of attack	ρ	fluid density
β	blade twist angle	B	number of blades
$\boldsymbol{r}$	source-receiver distance vector	b_c	blade chord
Δr	width of blade element	C_d	2D drag coefficient
ϕ	inflow angle	C_l	2D lift coefficient

$C_{\partial_r Q}$	sectional torque coefficient $C_{\partial_r Q} = \frac{\partial_r Q}{\rho n^2 D^4}$	V_A	axial component of free stream velocity
$C_{\partial_r T}$	sectional thrust coefficient $C_{\partial_r T} = \frac{\partial_r T}{\rho n^2 D^3}$	V_a	axial velocity at a blade section
L	aerodynamic source of loading noise	V_i	induced velocity at a blade section
n	rotational speed	V_t	tangential velocity at a blade section
p	fluid pressure	V_Z	in-plane component free stream velocity
Q	aerodynamic source of thickness noise	V_∞	free stream velocity
R	rotor radius; amplitude radius of an acoustic source	W	relative velocity at a blade section
		D	propeller diameter
r	radial position of a blade section	Q	torque
R^*	phase radius of an acoustic source	T	thrust

1. INTRODUCTION

The noise characteristics of a propeller operating in angular inflow differ significantly from those in uniform axial inflow conditions (D. B. Hanson & Parzych, 1993; D. Hanson, 1995; Romani, Grande, Avallone, Ragni, & Casalino, 2022a; Goyal, Sinnige, Ferreira, & Avallone, 2023; Jamaluddin, Celik, Baskaran, Rezgui, & Azarpeyvand, 2024). Two primary mechanisms contribute to these differences: the periodic variations in blade loading and the asymmetric phase modulation of noise sources' strength. The latter, referred as wobbling mode (D. Hanson, 1995; Carley, 2001), is purely acoustic in nature and is characterized by the periodic variation of the observer-source relative Mach number (D. Hanson, 1995; Carley, 2001). Accurate prediction of propeller noise at incidence necessitates unsteady aerodynamic data as an input and an acoustic formulation capable of capturing the effects of asymmetric phase modulation.

High-fidelity (HF) approaches, which typically couple a HF computational fluid dynamics (CFD) simulation method with the Ffowcs-Williams Hawkings (FW-H) acoustic analogy, are commonly used to predict propeller noise at incidence. Among these methods, HF CFD simulations performed using PowerFLOW®, based on the lattice-Boltzmann/very large eddy simulation (LB/VLES) method, have been successfully employed to analyze the aerodynamic performance of propellers. These analyses have been conducted for a range of configurations, from isolated single propellers (Casalino, Grande, Romani, Ragni, & Avallone, 2021; Romani et al., 2022a; Casalino, Romani, Pii, & Colombo, 2023) to full vehicle configurations (Casalino, van der Velden, & Romani, 2019), and under various operating conditions, from hover (Casalino et al., 2021) to forward flight (Yunus, Grande, Casalino, Avallone, & Ragni, 2022), including operations at incidence (Romani et al., 2022a). However, HF CFD simulations become prohibitively expensive when evaluating propeller performance across various operating conditions, especially when the main interest is assessing low-noise flight procedures. Therefore, there is a growing demand for computationally efficient yet reliable approaches to predict propeller noise under angular inflow conditions.

On the other hand, low-order (LO) approaches that couple an aerodynamic model based on blade element momentum theory (BEMT) with an aeroacoustic formulation have been proposed to calculate propeller noise. For instance, Casalino et al.(Casalino et al., 2021) developed and evaluated a LO approach within a benchmark activity for propeller aeroacoustics based on a small unmanned aerial vehicle (sUAV) through comparisons with wind

tunnel measurements and high-fidelity LB/VLES simulations. A compact dipole/monopole FW- H acoustic analogy formulation was used for tonal noise predictions. Accurate forces and tonal noise prediction were achieved using the LO approach. Recently, Yunus et al. (Yunus, von den Hoff, & Snellen, 2024) developed a LO approach to predict tonal noise from full electric propeller-driven aircraft at different operating conditions. Their LO approach employed Hanson's frequency domain acoustic formulation (D. B. Hanson, 1990) for the tonal noise prediction, and the approach was validated against HF simulation and outdoor measurements from several flyover events, including constant altitude level flight and several take-off flights with varying angular inflow conditions. Very satisfactory results were achieved between measurements, HF simulation, and LO predictions. However, the BEMT employed in these works assumes a uniform axial inflow and, hence, cannot account for contributions from unsteady loading from the propeller at incidence. In this work, the BEMT approach is extended by explicitly taking into account cross-flow variation on the rotor disk to calculate unsteady loading on a propeller operating in non-axial flow conditions.

From a theoretical standpoint, the solutions derived from the FW-H equations, which describe the noise radiation resulting from arbitrary motions of surfaces in a fluid, offer a comprehensive approach that considers the effects of various noise generation mechanisms. Notably, formulations such as Farassat 1 and 1A are extensively used to calculate the noise generated by rotating machines. However, both Farassat 1 and 1A formulations, without introducing algorithmic modification (Farassat, Dunn, & Spence, 1992), cannot be directly employed to account for non-axial inflow effects. Alternative to these corrected 1 and 1A formulations, Ghorbaniasl and Lacor (Ghorbaniasl & Lacor, 2012) introduced a time-domain (TD) moving medium formulation that explicitly considers the aerodynamic and acoustic effects of angular inflow with arbitrary direction. In an effort to enhance computational efficiency and applicability to transonic or supersonic tip speeds, Ghorbaniasl et al. (Ghorbaniasl, Huang, Siozos-Rousoulis, & Lacor, 2015) later proposed a frequency domain (FD) version of the TD moving medium formulation. In this study, the FD FW-H formulation derived by Ghorbaniasl et al. (Ghorbaniasl et al., 2015) is implemented and coupled with the extended BEMT model to predict propeller noise at incidence. This represents the first original contribution of this research.

Despite the existence of several LO approaches, their computational accuracy and efficiency have not been comprehensively examined. To address this gap, our study compares these two LO approaches in terms of computational accuracy and runtime with the HF simulation results established in the benchmark study conducted by Casalino et al. (Casalino et al., 2021). This comparison constitutes the second original contribution of our paper.

The remainder of the paper is organized as follows. In Section 2, an overview of low-order approaches is presented. The reference propeller and HF simulation setup are presented in Section III. The results are discussed in Section IV. Finally, conclusive remarks are reported in Section V.

2. Overview of low-order methodologies

In this study, two different low-order rotor aeroacoustic solvers are considered: LOPNOR, an in-house code developed by the leading author, and *Opty∂B*-BEMT/*Opty∂B*-PNOISE, part of the multi-purpose toolkit SIMULIA *Opty∂B*®. Both solvers are based on a two-step approach that first computes the aerodynamic loads and boundary layer properties along the span of a blade by means of a BEMT approach, and then computes the tonal noise by assuming a radial distribution of equivalent thickness and loading noise sources, and trailing-edge noise by means of a semi-analytical formulation based on the boundary layer properties in proximity of the trailing edge. In the current implementation, LOPNOR is only able to

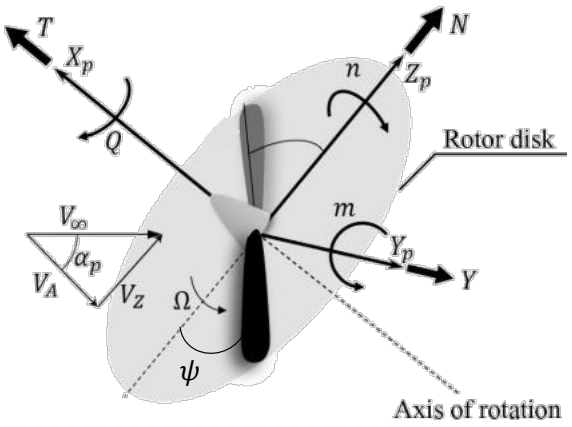

Figure 1: Illustration of propeller operating in angular inflow and propeller coordinate system (adapted from (Leng et al., 2021)).

compute the tonal noise radiation. The aerodynamic and aeroacoustic models used in both solvers are briefly outlined below.

2.1 LOPNOR

The LOPNOR solver is initially validated against HF simulation results and outdoor measurements (Yunus et al., 2024). The BEMT approach employed in LOPNOR assumes uniform axial inflow and, therefore, cannot account for unsteady (periodic) loadings from the propeller at incidence. This limitation is addressed by employing a quasi-steady BEMT approach, which will be outlined in the following section. Furthermore, the solutions of the frequency domain convected FW-H equation (Ghorbaniasl & Lacor, 2012) are implemented into LOPNOR, explicitly accounting for unsteady loading and asymmetric phase modulation effects of propeller noise at incidence.

2.1.1 Aerodynamic model

When a propeller operates at angular inflow, the freestream velocity V_∞ is decomposed into two components: V_A along the rotation axis and V_Z in the rotor disk plane, with respect to the propeller incidence angle and rotational axis, as illustrated in Fig. 1. The propeller coordinate takes the rotor center as origin, with the X-axis being the rotating axis and the Z-axis aligned with V_Z. Due to the nonzero incidence angle, the axisymmetric assumption is no longer valid. The local velocity and angle of attack for each blade section vary with the azimuthal position ψ on the rotor disk. Consequently, an imbalance of lift and drag forces occurs on a blade section over a full revolution. These imbalances create a pitching moment m around the Y_p axis and a rolling moment n around the Z_p axis. Additionally, the axial component of the freestream, $V_A = V_\infty \cos(\alpha_P)$, causes a reduced freestream velocity effect in the axial direction. Meanwhile, the in-plane component, $V_Z = V_\infty \sin(\psi)$, induces a variation in cross flow as a function of the blade azimuthal position, ψ.

The extended BEMT analysis for nonzero α_P follows the same methodology as the axial inflow, as reported in (Casalino et al., 2021; Yunus et al., 2024). However, in this case, most flow components vary with ψ, as illustrated in Fig. 2. For instance, on the advancing side of the propeller, where $0 < \psi < \pi$, the in-plane component of the freestream V_Z aligns with the direction of blade rotation. This alignment increases the tangential velocity at a blade element, expressed as $V_t(\psi) = r\Omega + V_\infty \sin\alpha_P \sin\psi - V_{iT}$, with V_{iT} representing the tangential component of the induced velocity. The axial velocity on the advancing blade side is given by $V_a(\psi) = V_\infty \cos\alpha_P + V_{iA}$ and is independent of ψ. Consequently, the local relative wind speed $W(\psi) = \sqrt{V_a^2 + V_t^2}$ increases. The inflow angle $\phi(\psi)$ on the advancing side is then expressed

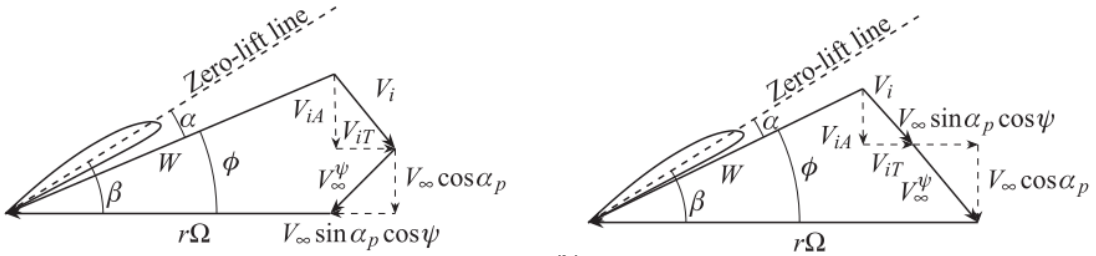

(a) Advancing blade. **(b)** Retreating blade.

Figure 2: Flow directions of advancing and retreating blade sections (Leng et al., 2021).

as:

$$\phi(\psi) = \tan^{-1}\left(\frac{V_\infty \cos\alpha_P + V_{iA}}{r\Omega + V_\infty \sin\alpha_P \sin\psi - V_{iT}}\right). \tag{1}$$

On the retreating side of the propeller, as depicted in Fig. 2b, where $\pi < \psi < 2\pi$, the inplane component of the freestream, V_Z, opposes the direction of blade rotation. This opposing direction reduces the tangential velocity, $V_t(\psi) = r\Omega - V_\infty \sin\alpha_P \sin\psi - V_{iT}$, and consequently, the local relative wind speed, $W(\psi)$. It is noted that the axial velocity, $V_a(\psi)$, at a blade section remains unchanged compared to the advancing side. The inflow angle is determined by the following relation:

$$\phi(\psi) = \tan^{-1}\left(\frac{V_\infty \cos\alpha_P + V_{iA}}{r\Omega - V_\infty \sin\alpha_P \sin\psi - V_{iT}}\right) \tag{2}$$

Following the BEMT formulation in the axial inflow case (Yunus et al., 2024), the sectional thrust and torque on an annulus of width Δr can be obtained by establishing a BEMT balance for the angular inflow case as follows:

$$\Delta T = 4\pi r \rho_0 (V_\infty \cos\alpha_P + V_{iA}) V_{iA} \Delta r = \frac{1}{2}\rho_o W^2 b_c (C_l \cos\phi - C_d \sin\phi) B \Delta r \tag{3}$$

$$\Delta Q = 4\pi r^3 \rho_0 (V_\infty \cos\alpha_P + V_{iA}) V_{iT} \Delta r = \frac{1}{2}\rho_o W^2 b_c (C_l \cos\phi + C_d \sin\phi) B r \Delta r, \tag{4}$$

where r is the radius of the blade section and b_c is the blade sectional chord, B is the number of blades. $W(\psi) = \sqrt{V_a^2 + V_t^2}$ is the total velocity seen by every radial section at ψ. The local angle of attack as a result of the geometrical blade section pitch angle β and inflow angle ϕ is $\alpha(\psi) = \beta - \phi(\psi)$. The Eq. 3-4 are solved in an iterative procedure with initial guesses for the axial and tangential induced velocities. Upon determining the Reynolds number and angle of attack seen by a blade element at each ψ, the associated lift and drag coefficients C_l and C_d are interpolated from the 2D meshes of $C_l(Re, \alpha)$ and $C_d(Re, \alpha)$ values at each ψ established in a prior step.

For the aeroacoustic solver which will be outlined in the following section, the aerodynamic sources for the thickness (Q) and the loading (L) type noise are given by (Ghorbaniasl & Lacor, 2012)

$$\begin{aligned} Q &= \rho[u_n - (v_n - V_{\infty n})] + \rho_0 (v_n - V_{\infty n}) \\ L_i &= \rho u_i [u_n - (v_n - V_{\infty n})] + P_{ij}\hat{n}_j, \end{aligned} \tag{5}$$

where $V_\infty n = V_{\infty i}\hat{n}_i$, and $\hat{\boldsymbol{n}}$ is unit outward normal vector to the data surface on which flow quantities are sampled. $V_{\infty i}$ indicates the components of uniform inflow velocity in a Cartesian

coordinate system with $i = 1,2,3$. The term $P_{ij} = (p - p_0)\delta_{ij} - \sigma_{ij}$ denotes the compressive stress tensor, where p_0 is the fluid pressure at rest, δ_{ij} represents the Kronecker delta, and σ_{ij} is the viscous stress tensor. The velocity of the data surface is given by $v_n = v_i \hat{n} i$. Since the blade surface is regarded as the moving data surface, the local fluid velocity $u_n = u_i \hat{n}_i$ on the surface equals the relative velocity of the blade $u_n = v_n - V_{\infty n}$. Consequently, the source term Q is simplified to $Q = \rho_0(v_n - V_{\infty n})$. For inviscid flow, the expression of L_i takes the form $L_i = (p - p_0)\delta_{ij}\hat{n}_j$. It is worth noting that the 3D blade geometry and aerodynamic force distributions across spanwise, chordwise, and azimuthal directions are considered in the present solver. Hereafter, the solver is denoted as LOPNOR-BEMT.

2.1.2 Aeroacoustic model

The FD solution of the convected FW-H equation, derived by Ghorbaniasl *et al.*(Ghorbaniasl et al., 2015), for surface sources in motion that accounts for the flow incidence effects, is implemented in this work. The loading (p'_L) and thickness (p'_T) components of the tonal noise read:

$$4\pi p'_L(\boldsymbol{x},\Omega,\boldsymbol{M}_\infty) = \int_S \int_{-\infty}^{t} \left(\frac{ikF_R}{R^*} + \frac{F_{R^*}}{R^{*2}} \right) e^{-ikR} e^{-i\Omega\tau} d\tau dS \tag{6}$$

$$4\pi p'_T(\boldsymbol{x},\Omega,\boldsymbol{M}_\infty) = \int_S \int_{-\infty}^{t} i\Omega \frac{Q}{R^*} e^{-ikR} e^{-i\Omega\tau} d\tau dS \tag{7}$$

where $F_i = L_i - QU_{\infty i}$, $F_R = F_i \hat{R}_i$ and $F_{R^*} = F_i \hat{R}^*_i$. $\boldsymbol{M}_\infty = \boldsymbol{V}_\infty / c_0$, with components of $M_{\infty i} = V_\infty i / c_0$ in a Cartesian coordinate system with $i = 1,2,3$, $\boldsymbol{V}_\infty$ is the uniform inflow velocity of arbitrary orientation. $\gamma = 1/(1 - |\boldsymbol{M}_\infty|^2)$, $R^* = \frac{1}{\gamma}\sqrt{r^2 + \gamma^2(\boldsymbol{M}_\infty \cdot \boldsymbol{r})^2}$ and $R = \gamma^2(R^* - \boldsymbol{M}_\infty \cdot \boldsymbol{r})$ represent the amplitude radius and the phase radius in a uniform mean flow of arbitrary direction, respectively. $\hat{R}_i = \partial R / \partial x_i$, $\hat{R}^*_i = \partial R^* / \partial x_i$ and S represents the blade surface, $\boldsymbol{x}$ contains the receiver coordinates, Ω is the source frequency, τ is the source time and $\boldsymbol{r}$ is the source receiver distance. More details of the derivation can be found in (Ghorbaniasl et al., 2015).

The aerodynamic and acoustic effects of flow incidence are explicitly considered in this formulation. A notable distinction of this formulation, in contrast to the time-domain approach presented in (Ghorbaniasl & Lacor, 2012), is its freedom from the Doppler singularity and simpler expression of acoustic source terms compared to those in the time-domain formulation. The calculation of the total pressure signal at a receiver point, incorporating contributions from both thickness and loading noise, is determined by the following relation (Magliozzi, Hanson, & Amiet, 1991).

$$p'(\boldsymbol{x},t,M_\infty) = \sum_{m=-\infty}^{\infty} [p'_L(\boldsymbol{x},\Omega,\boldsymbol{M}_\infty) + p'_T(\boldsymbol{x},\Omega,\boldsymbol{M}_\infty)] e^{-imB\Omega t}, \tag{8}$$

where t is the receiver time and m is the acoustic harmonic number. In the following section, this solver is referred to as LOPNOR-FWH. It should be noted that the chordwise distribution of acoustic sources is considered by LOPNOR-FWH. Additionally, being a frequency-domain solver, this emphasizes the primary distinction between LOPNOR-FWH and *Opty∂B*-PNOISE, as outlined in the following section.

In the current version of the LOPNOR-FWH solver, single-core computation is implemented. Therefore, unlike *Opty∂B*-PNOISE, concurrent execution across multiple cores is currently not supported. Implementation of concurrent execution is underway and will be incorporated into the next release of the solver. Computations are performed on a Macintosh laptop with an Intel Core i9 2.3 GHz processor.

2.2 Opty∂B

The rotor aeroacoustic LO model available in *Opty∂B* has been described in (Casalino et al., 2021). Similarly to LOPNOR, it is based on a BEMT model supplied by *Opty∂B*-BEMT, with sectional aerodynamic polars and boundary layer properties computed with an embedded proprietary viscous panel code based on (Drela & Giles, 1987) method. The radial distribution of lift and drag coefficients are then converted by *Opty∂B*-PNOISE into constant pressure distributions on the three faces of a radial wedge of the same sectional area of the original blade, following the compact monopole/dipole formulation put forward in (Casalino, Barbarino, & Visingardi, 2011). In order to take into account the effects due to sweep/lean angular deflection of the blades, the original definition of the leading- and trailing-edge line is kept in the surrogate geometrical model of the blade. Moreover, as recently shown in (Pii, Casalino, Romani, & Singal, 2024), the model is able to account for a circumferential variation of the blade geometry and angular spacing. A time-domain acoustic analogy calculation is then applied by automatically executing *Opty∂B*-FOXWHAWK, which makes use of a forward-time formulation of Farassat 1A formulation (Casalino, 2003). This results in periodic noise signals due to the fluid displacement and to the steady loading applied on the blades. In the presence of a non-axial flow, the sectional upwash velocity is evaluated along the rotor revolution, subsequently Fourier-transformed in time, and finally used to calculate an unsteady lift fluctuation by means of a Kármán-Sears model. The corresponding pressure distribution is added to the steady contribution prior the FW-H calculation. This results in periodic noise signals due to both steady and unsteady loading applied on the blades. A stochastic inflow turbulence model can be also used to calculate turbulent unsteady loading, but this model is not used in the present study. The noise radiated by the turbulent boundary layer is finally computed by means of a finite-chord thin airfoil semi-analytical model, with leading-edge acoustic back scattering taken into account (Roger & Moreau, 2005), a Corcos model to estimate the spanwise correlation length, and the wall-pressure spectrum computed using a revisited version of (Schlinker & Amiet, 1981) model, fed with boundary layer properties extracted at 97.5% and 95.0% of the chord on the suction and pressure side, respectively. Optionally, the broadband noise spectra can be converted into stochastic signal contributions added to the periodic signals.

3. REFERENCE PROPELLER AND LB/VLES NUMERICAL SETUP

The geometry herein considered is a two-bladed propeller designed at TU-Delft (Fig. 3a) and extensively examined in previous experimental (Grande, Romani, Ragni, Avallone, & Casalino, 2022; Grande, Ragni, Avallone, & Casalino, 2022) and numerical (Casalino et al., 2021; Romani et al., 2022a; Casalino, Romani, Zhang, & Chen, 2022; Casalino et al., 2023) studies. It is characterized by a radius $R = 0.15$ m and NACA 4412 airfoil sections, which are merged with the propeller hub by elliptical sections (for $r/R < 0.2$). The airfoil chord and twist spanwise distributions provided in Fig. 3b. The propeller hub radius is 1.25 cm and connected to a nacelle of 5 cm diameter and 52 cm length.

In this work, the propeller is operated at fixed angular velocity ($n = 83.33$ RPS, i.e. $\Omega = 523.6$ rad/s) and free-stream velocity of 10 m/s, resulting in an advance ratio $J = 0.4$ (where $J = V_\infty/(nD)$, with n denoting the revolution per seconds and D the propeller diameter). The resulting tip Mach number is 0.23 and the Reynolds number based on the chord at 75% of the radius is about $9 \cdot 10^4$. Two different values of the propeller yaw angle are considered to investigate the effects of an angular inflow, namely $\alpha_P = 0^\circ$ and 15°. The free-stream static pressure and temperature considered are $p_\infty = 99000$ Pa and $T_\infty = 293.15$ K, respectively.

Figure 4a shows the PowerFLOW computational setup which is employed to produce high-fidelity LB/VLES simulation data (Romani et al., 2022a) for the assessment of the low-

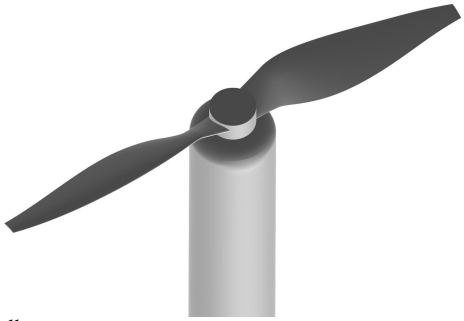

(a) Propeller geometry.

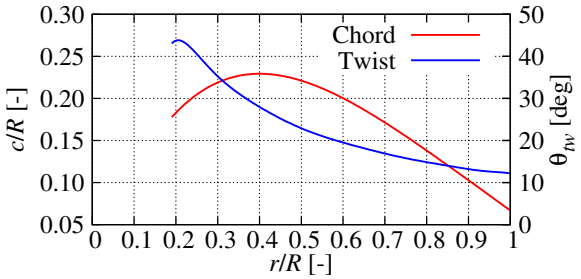

(b) Chord and twist distributions.

Figure 3: Propeller geometry, airfoil chord and twist spanwise distributions.

order methodologies herein proposed. The fluid domain is a spherical volume of $325D$ radius centered around the propeller. Free-stream static pressure and velocity, and turbulence intensity of 0.1% of the free-stream velocity are prescribed on its outer boundary. The experimental anechoic wind tunnel geometry is not modeled in the computational setup. However, an acoustic sponge is used to dissipate the out-going acoustic waves and minimize the backward reflection from the outer boundary, thus reproducing a digital anechoic environment. The acoustic sponge is defined by two concentric spheres of radius $15D$ and $55D$, respectively, centered around the propeller. The fluid kinematic viscosity is gradually increased starting from its physical value within the inner sphere, up to an artificial value two orders of magnitude higher outside the outer one. A zig-zag transition trip is employed on the suction side of the blade to drive the conventional LB/VLES scheme switching from turbulence modeling to scale-resolving behavior, thus allowing the formation of resolved turbulent structures within the boundary-layer for the sake of turbulent boundary-layer trailing-edge noise broadband calculation. The zig-zag trip is characterized by a thickness of 0.17 mm, amplitude and wavelength of 0.9 mm, and is placed at 25% of the chord on the suction side of the blade for $r/R > 0.2$ (4b). No trip is placed on the blade pressure side, since no laminar-to-turbulent boundary layer transition is expected to occur based on *Opty∂B*-BEMT computations. This approach has been successfully validated in previous studies on the prediction of the performances and tonal/broadband noise radiation of a low-speed propeller in axial and non axial inflow conditions (Casalino et al., 2021; Romani, Grande, Avallone, Ragni, & Casalino, 2022b; Romani et al., 2022a). It is worth mentioning that these simulations have been performed before the introduction of a new VLES model in PowerFLOW that, when the mesh resolution is sufficiently high, promotes a spontaneous transition between modelled to resolved turbulence (Casalino et al., 2022) in the boundary layer, without the need of a physical trip.

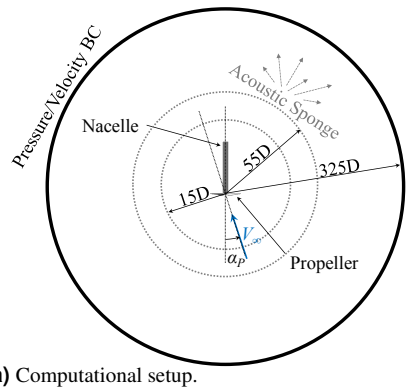

(a) Computational setup.

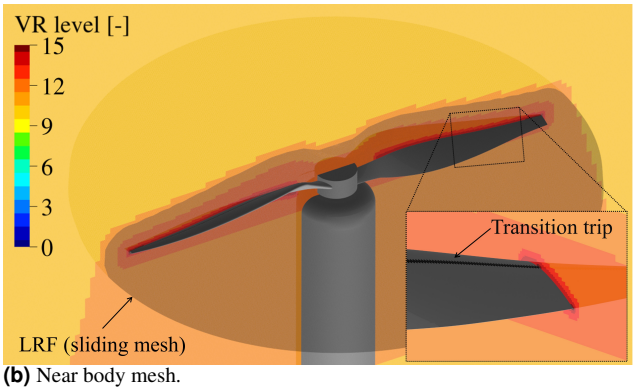

(b) Near body mesh.

Figure 4: Sketch of computational setup (not drawn to scale) and near body grid.

Figure 4b shows the details of the computational setup and grid close to the propeller

geometry. The propeller and hub are encompassed by a volume of revolution that defines the Local Reference Frame (LRF), i.e. the rotating sliding mesh domain used to enable the propeller rotation. The solid FW-H integration surface used to compute the far-field noise radiation coincides with the propeller, hub and nacelle surfaces. A total of 16 Variable Resolution (VR) regions are used to discretize the whole fluid domain, with the finest resolution level (VR15) placed around the blade trip and trailing-edge. A resolution of 200 voxels along the mean chord (22.85 mm) is used in the second finest resolution level (VR14), resulting in a smallest voxel size of 0.06 mm, a mean $y+ \approx 5$ on the blade surface and an overall mesh size of 107 million voxels. The computational cost is 840 CPUh/rev on a 430 cores cluster with Intel Xeon CPU E5-2697 2.6 GHz. The whole fluid domain is initialized with the instantaneous flow solution from a statistically converged coarser simulation. Hence, after a settling time corresponding to 2 propeller revolutions, the sampling of relevant flow data is started for 10 additional revolutions. Acoustic data is sampled at 365 kHz with spatial averaging of 0.5 mm on the solid FW-H integration surface. Fourier transformed data is obtained with 2 Welch blocks, 50% overlap and Hanning windowing, corresponding to a bandwidth of 16.6 Hz (BPF 0.1).

4. RESULTS

4.1 Prediction of unsteady thrust and torque distributions

The prediction capabilities of the unsteady thrust and torque distributions on the rotor disk of the LO methods are investigated by comparing results with the ones obtained using the HF simulation approach. The fluctuating, mean-removed, sectional thrust and torque distributions, $C'_{\partial rT}$ and $C'_{\partial rQ}$, are compared in Fig. 5. As expected, due to the non-axial flow condition, a classical 1-rev asymmetric pattern of the disk loading is obtained. More specifically, two distinctive features are visible in the HF and *Opty∂B*-PNOISE results. First, the highest and lowest values occur slightly after $\psi = 90°$ and $\psi = 270°$, respectively. This is due to the delayed blade aerodynamic response to the upwash velocity variation that, in *Opty∂B*-PNOISE, it is taken into account by the Kármán-Sears model. Second, variations on the advancing side are higher than those on the retreating side, primarily due to the larger increase in the local airfoil angle of attack on the advancing side compared to its reduction on the retreating side (Romani et al., 2022a). Since LOPNOR-BEMT is based on a quasi-steady aerodynamic approximation, it predicts the maximum and minimum forces at $\psi = 90°$ and $\psi = 270°$, receptively, without any delay respect to the upwash velocity variation. However, LOPNOR-BEMT accurately captures the second feature.

The HF results exhibit the presence of some irregularities that are due to two reasons. The first one is the presence of the trip in the simulations, which generates local flow fluctuations and makes the sectional load extraction more difficult. The second is related to the sectional load extraction procedure that was not very robust at the time when these loads were extracted. A new procedure is currently in place and it will be used in future to update these results.

4.2 Prediction of far-field noise & PWL

4.2.1 Far-field noise spectra

The far-field noise prediction capability of the LO approaches is examined in this section by comparing the LO predictions against data from the HF approach and wind tunnel measurements. Three different microphones in the free-stream coordinate system, as illustrated in Fig. 6, are considered. Mic. 3 (0.6, 1.2, 0.0) m and Mic. 11 (-0.6, 1.2, 0.0) m are positioned outside the propeller plane ($\alpha_P = 0°$), while Mic. 7 (0.0, 1.2, 0.0) m is located

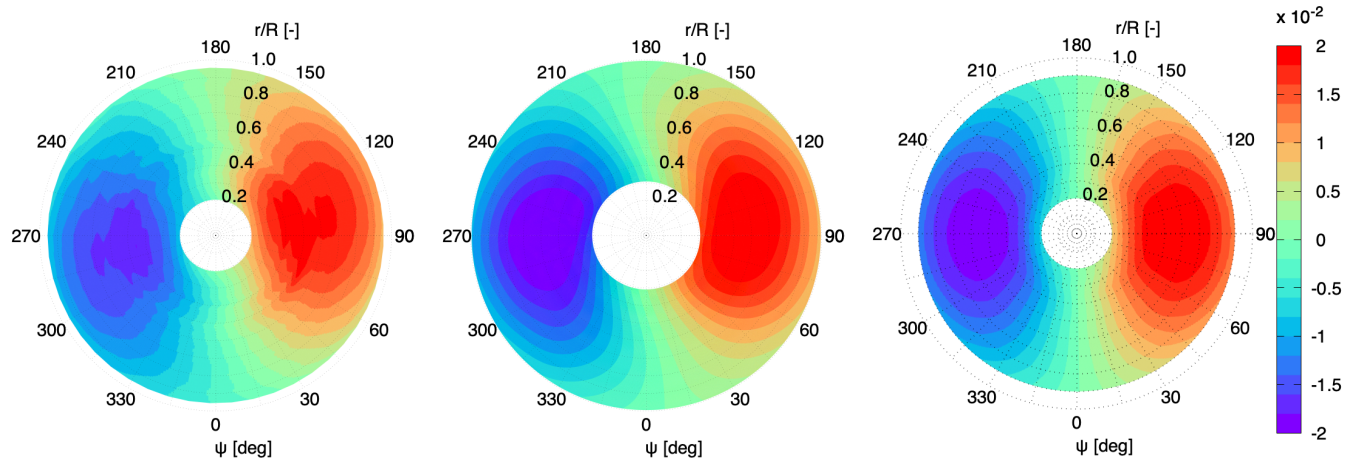

(a) Thrust coefficient, HF simulation. **(b)** Thrust coefficient, *Opty∂B*-BEMT. **(c)** Thrust coefficient, LOPNOR-BEMT.

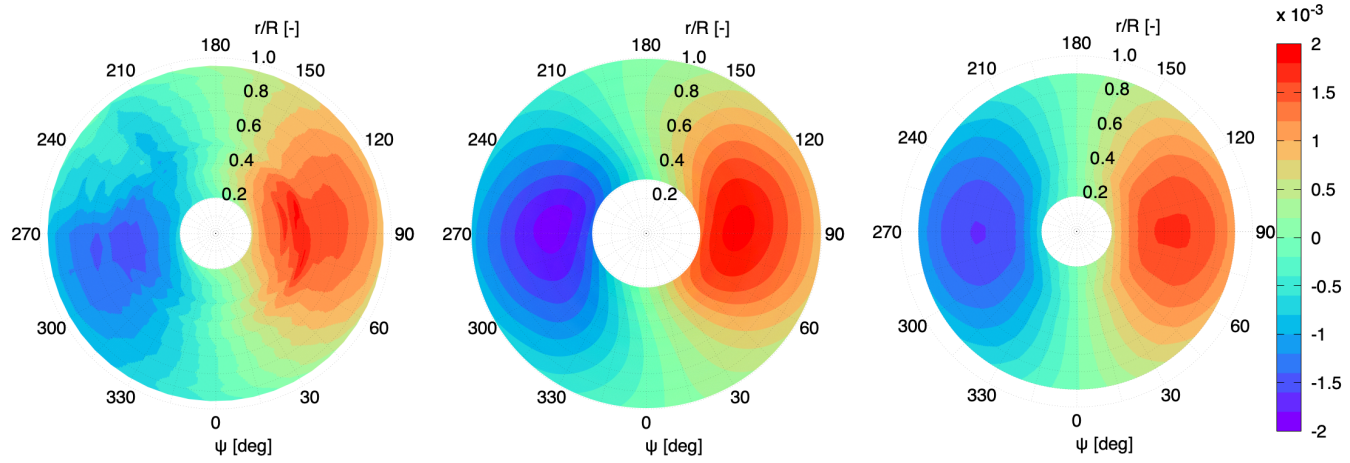

(d) Torque coefficient, HF simulation. **(e)** Torque coefficient, *Opty∂B*-BEMT. **(f)** Torque coefficient, LOPNOR-BEMT.

Figure 5: Fluctuating thrust and torque coefficient for the $\alpha_P = 15°$ case.

within the propeller plane ($\alpha_P = 0°$). The far-field noise spectra are computed for all micro-

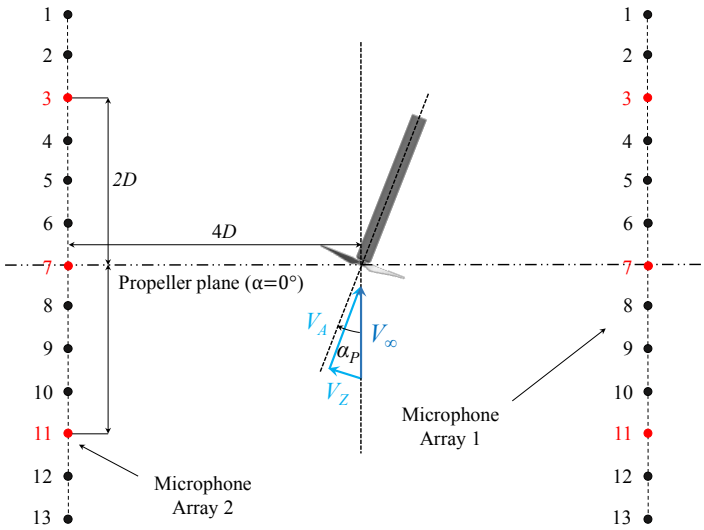

Figure 6: Sketch of the microphone array used of far-field noise computation.

phones on array 1 for both axial and angular inflow cases and compared against data from HF and experimental measurements, as shown in Fig. 7. For $\alpha_P = 0°$ at Mic. 3, LOPNOR-FWH showed excellent agreement with the measurement at the first and second harmonics of the BPF, while *Opty∂B* underpredicts the tonal peaks at both BPF harmonics. As discussed

in (Casalino et al., 2023), this can be due to some spectral contamination in the measurements due to effect of flow reticulation in the test room. At Mic. 7, both LOPNOR-FWH and *Opty∂B* showed excellent agreement at the first BPF with the measurement and HF data but underpredict the tonal peaks of the second BPF of the measurement, while showing good agreement with HF data. At Mic. 11, predictions from both LO approaches showed very good agreement with the measurement and HF data at both BPF harmonics. At all three microphones, *Opty∂B* exhibited strong agreement with the HF results across all considered harmonic numbers. In contrast, LOPNOR-FWH only showed levels up to the third harmonics, with significantly lower values at the third harmonics of the BPF due to its lack of broadband noise calculation capability. This limitation will be addressed in future studies.
For $\alpha_P = 15°$, an overall increase in noise levels at all microphones is observed compared to $\alpha_P = 0°$, particularly at Mic. 7. LOPNOR-FWH demonstrated excellent agreement with both the measurements and HF data for the first BPF at all microphones. In contrast, *Opty∂B* slightly underpredicts the tonal peaks at the first BPF. At the second BPF, LOPNOR-FWH significantly underpredicts the tonal peaks at Mic. 3 and Mic. 7, although this underprediction was slightly less pronounced at Mic. 7. Conversely, *Opty∂B* showed excellent agreement with the measurement data at the second harmonics of the BPF across all microphones. Unlike the axial inflow condition with $\alpha_P = 0°$, LOPNOR-FWH predicted the tonal peaks at the third BPF reasonably well compared to the measurements. It also showed excellent agreement with the HF data at Mic. 3 and Mic. 7 and slightly overpredicted the HF results at Mic. 11 while maintaining excellent agreement with the measurement data. Similarly, *Opty∂B* displayed excellent agreement with the HF data across all higher harmonics at Mic. 3, reasonable agreement at Mic. 7, and overprediction at Mic. 11. Notably, LOPNOR-FWH exhibited very good agreement with *Opty∂B* and reasonable agreement with the HF data across all harmonic numbers at Mic 7, while lower prediction at Mic. 3 and Mic. 11. This suggests that tonal noise from unsteady loading becomes a significant contributor at higher harmonics, as evident from LOPNOR-FWH's predictions across all microphones.

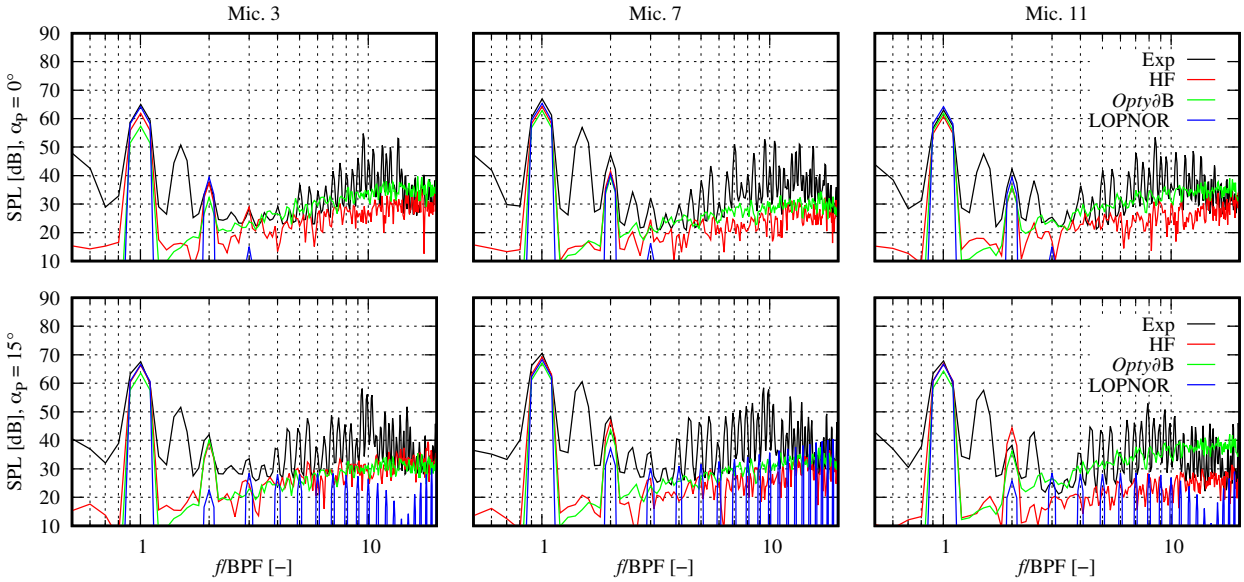

Figure 7: Far-field noise spectra for three microphones on array 1 and both axial and non-axial flow conditions.

The far-field noise spectra for microphones distributed on array 2 are shown in Fig. 8. For axial inflow conditions with $\alpha_P = 0°$, the same trend observed for the microphones on array 1 is evident. Under angular inflow conditions with $\alpha_P = 15°$, a noticeable reduction in the tonal noise level at the first two harmonics of the BPF is observed across all microphones. Both LO approaches capture this trend well. At Mic. 3, LOPNOR-FWH shows excellent agreement with the HD data at the first BPF, slightly underpredicting the measurement data, and pre-

dicts well the measurement data at the second harmonic with a clear underprediction of the HF data. *Opty∂B* also shows very good agreement with the HF data, slightly underpredicting the measurement data at the first BPF, and excellent agreement with the HF results at the second BPF, although with a considerable underprediction of the measurement data. From the third BPF onwards, LOPNOR-FWH underpredicts the measurements but aligns reasonably well with the HF data across all harmonic numbers. Conversely, *Opty∂B* shows strong agreement with the measurements at higher harmonics, though it overpredicts the HF data at these levels. At Mic. 7, both LOPNOR-FWH and *Opty∂B* align excellently with the HF data, though they underpredict the measurement results at the first BPF. This trend continues at the second BPF. From the third BPF onwards, both approaches show good agreement with the HF data across all harmonics, while underpredicting the measurement results at higher harmonics. At Mic. 11, LOPNOR-FWH accurately captures the tonal peak of the measurement at the first BPF, whereas *Opty∂B* slightly overpredicts it. At the second BPF, both LOPNOR-FWH and *Opty∂B* underpredict the measurement data and overpredict the HF results. LOPNOR-FWH shows reasonable agreement with the HF data up to the 9th harmonic, while *Opty∂B* demonstrates excellent agreement with the HF results across all harmonics.

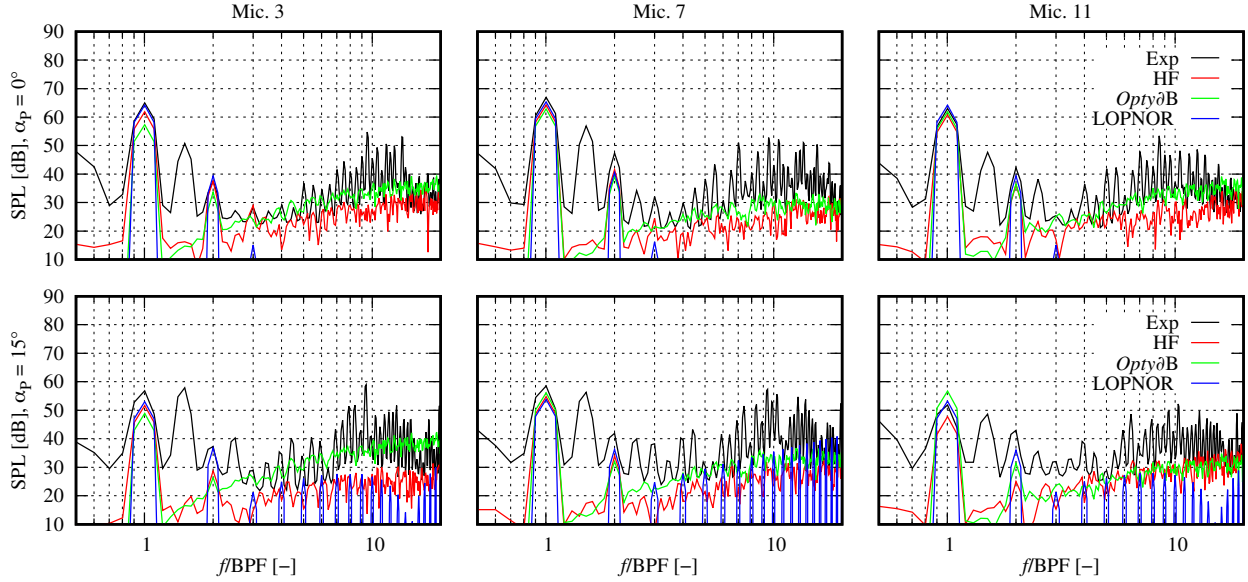

Figure 8: Far-field noise spectra for three microphones on array 2 and both axial and non-axial flow conditions.

It should be noted that all microphones in both arrays exhibited considerable tonal peaks at BPF 0.5, 1.5, and 2.5. These peaks are attributed to the imperfect balance of the blade loading and the noise from the loaded electric motor. As this study exclusively focuses on propeller noise, the modeling of noise due to the imbalance of blade loading and the loaded electric motor is not considered. Although tracking the specific reasons of discrepancy in tone level prediction is not the final goal of this work, it should be mentioned that the HF results have been obtained by neglecting the mean-flow convection effects, under the assumption that the sound propagation mostly occurs in quiescent conditions outside the wind-tunnel jet. On the contrary, the LF predictions take into account a free-stream convection. As a matter of fact, comparisons between Hf and *Opty∂B*-PNOISE results for the same rotor in hover conditions and higher rotational speed carried out in (Pereira, Ragni, Romani, & Casalino, n.d.) exhibit an almost perfect agreement of tonal levels.

The observed trend indicates that when the propeller is tilted with respect to the freestream flow, noise levels at the first and second harmonics of the Blade Passage Frequency (BPF) are significantly impacted. Noise levels at these two BPFs increase at the microphones from which the propeller tilts away and decrease at those towards which it tilts. This trend is well-predicted by both LO solvers. Notably, at non-zero incidence, tonal noise from un-

steady loading becomes a significant contributor to the lower to mid-frequency range, as clearly shown in the LOPNOR-FWH predictions. The contributions from unsteady loading are comparable to those of other broadband noise sources. This trend will be investigated in a future study. It is noted that *Opty∂B* demonstrated reasonable agreement with the HF data across all harmonics, except for an overprediction at Mic. 11 on array 1 and Mic. 3 on array 2 under the angular inflow condition.

As a conclusive remark of this subsection, it is worth arguing that, in general, rotor noise tones are submitted to several uncertainties, both in measurements and predictions. Theretofore, a meaningful one-to-one tonal level comparison would require a characterization of the uncertainties associated with every process, as recently carried out by (Pereira et al., n.d.).

4.2.2 Noise power level

The investigation of the predictions from the two LO approaches for propeller noise at incidence, considering the effects of angular inflow on the resulting radiated noise field, concludes with a comparison of source power level predictions. The source power level (PWL) represents the acoustic energy generated by the propeller, independent of distance and observation angle. The PWL spectrum is evaluated by integrating the power spectral densities (PSDs) of the total acoustic signature computed by the FW-H acoustic solvers considering a spherical array with a radius of 10 times of blade radius, centered around the propeller hub, using the following formula:

$$\mathrm{PWL}(f) = \int_0^{2\pi}\int_0^{2\pi} R_s^2 \sin(\theta) \frac{[1+M_\infty \cos(\theta)]^2 \mathrm{PSD}(f,\phi,\theta)}{2\rho_0 c_0} \mathrm{d}\phi \mathrm{d}\theta, \tag{9}$$

where f is the frequency, R_s is the sphere radius, θ and ϕ are the angular coordinates of the source sphere. While M_∞, ρ_0 and c_0 are the free-stream Mach number, density and speed of sound. A total of 375 microphones, 15 parallel and 25 meridian points, are used for the PWL calculation.

The PWLs computed with both LO solvers are compared against HF data for axial ($\alpha_P = 0^\circ$) and angular inflow ($\alpha_P = 15^\circ$) conditions, as depicted in Fig. 9. For the axial inflow condition, both LOPNOR-FWH and *Opty∂B* slightly overpredict the first BPF tone compared to HF, while showing much better agreement at the second BPF. Notably, *Opty∂B* exhibits excellent agreement with HF data across the entire frequency range. Under the angular inflow condition ($\alpha_P = 15^\circ$), predictions at the first BPF improve significantly compared to the axial inflow condition. However, LOPNOR-FWH overpredicts the HF result at the second BPF, whereas this overprediction is smaller with *Opty∂B* , which shows better overall agreement with the HF data compared to LOPNOR-FWH .

The predictions of PWL suggest that noise emissions of the propeller at incidence were accurately predicted by both LO approaches, which can be efficiently applied for noise prediction at incidence with significantly reduced computation time, as detailed in Table 1. The CPU time for the broadband *Opty∂B*-PNOISE calculation includes the noise spectra calculation and the broadband signal auralization prior merging of the tonal and broadband signals. This second step, which is indeed an optional one, is the most expensive part of the broadband noise signals calculation. Moreover, in order to have a high frequency sampling of the synthetic broadband noise signals, the *Opty∂B*-PNOISE calculations were performed with 500 time-steps per blade passing period. For the sake of consistency, the same time step was used for the tonal noise calculations. Since a much lower value would be sufficient to recover the proper tonal noise levels, the reported CPU time for tonal noise calculations are much higher than what is really needed for tonal noise predictions. On the other hand, the CPU time of LOPNOR-FWH for the axial flow condition reflects a reasonable computational

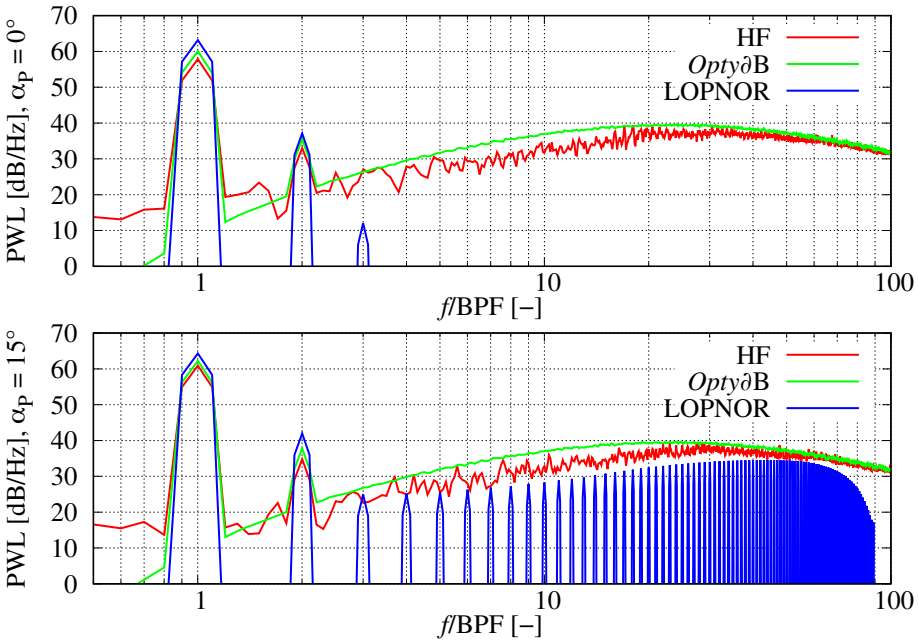

Figure 9: Comparison between Power Watt Level (PWL) spectra from HF simulation, *Opty∂B* and LOPNOR for $\alpha_P = 0°$ and $\alpha_P = 15°$.

time for a frequency domain solver typically used for propeller tonal noise calculations, considering only three harmonics. However, for the non-axial case, the CPU time increased significantly due to the consideration of 101 harmonics to cover the full frequency range, ensuring consistency with the other two predictions on the PWL noise calculation. Therefore, a direct comparison of CPU time with *Opty∂B*-PNOISE for the non-axial condition does not reflect reality. It is however interesting to report these CPU time figures for the sake of future reference.

Table 1: Comparison of CPU time between LOPNOR-FWH and *Opty∂B*-PNOISE for 375 microphones.

Solver	α_P	CPU cores	CPU time (tonal) [s]	CPU time (broadband) [s]
Opty∂B-PNOISE	0°	10	57	914
LOPNOR-FWH	0°	1	40	N/A
Opty∂B-PNOISE	15°	10	64	924
LOPNOR-FWH	15°	1	12204	N/A

5. Conclusion

The accuracy and computational efficiency of two low-order methods for propeller tonal and broadband noise prediction in both axial and non-axial flow scenarios were investigated. Experimental data and scale-resolving LB/VLES CFD results for a two-bladed small unmanned aerial system under transitional boundary layer conditions were used as a reference. The following conclusions are drawn:

- The comparison of unsteady loading predictions indicates that, both LO approaches provide satisfactory predictions of the unsteady thrust and torque variations in non-axial flow conditions.

- For far-field noise spectra predictions, both methods show excellent agreement with high-frequency (HF) and measurement data in axial conditions. *Opty∂B* accurately predicts broadband noise at higher harmonics, while LOPNOR lacks this capability. In non-axial conditions, both methods capture significant increases and decreases in noise levels at the first harmonics of BPF across all microphones. However, LOPNOR systematically underpredicts the tonal peak at the second BPF on array 1, while *Opty∂B* does so on array 2. These fluctuations in predictions at the second BPF likely stem from the fidelity of predicted unsteady loading.

- Under non-axial conditions, tonal noise from unsteady loading can substantially contribute to the lower to mid frequency range, comparable to other broadband noise sources in this range.

- *Opty∂B* accurately predicts PWL across all frequencies with slight overprediction up to the 11th BPF, while LOPNOR accurately predicts the first two BPF tonal peaks in axial conditions. However, for non-axial conditions, LOPNOR considerably overpredicts the second BPF, while capturing the trend at higher harmonics.

- For the tonal noise calculation, both approaches achieve a significant and similar speedup.

The results suggest that both approaches can be effectively utilized for predicting tonal noise of propellers under non-axial inflow conditions with acceptable accuracy and significant reduction in computation time. Additionally, *Opty∂B* can be employed to predict broadband noise across the entire frequency range. The dominance of tonal noise from unsteady loading in the lower to mid-frequency range, compared to other broadband noise sources, will be investigated in future work.

Finally, new LB/VLES high-fidelity simulations will be performed in the future using a recently released extension of the PowerFLOW VLES model (Casalino et al., 2022, 2023), which was developed to address low-Reynolds number flows, to incorporate the effects of the laminar separation bubble on the aerodynamic loading and thus providing a more reliable benchmark for the assessment of the LO methodologies.

REFERENCES

Carley, M. (2001, 6). The structure of wobbling sound fields. *Journal of Sound and Vibration*, *244*, 1-19. doi: 10.1006/jsvi.2000.3451

Casalino, D. (2003). An advanced time approach for acoustic analogy predictions. *Journal of Sound and Vibration*, *261*(4), 583–612.

Casalino, D., Barbarino, M., & Visingardi, A. (2011). Simulation of helicopter community noise in complex urban geometry. *AIAA Journal*, *48*(8), 1614–1624.

Casalino, D., Grande, E., Romani, G., Ragni, D., & Avallone, F. (2021). Definition of a benchmark for low reynolds number propeller aeroacoustics. *Aerospace Science and Technology*, *113*, 106707.

Casalino, D., Romani, G., Pii, L. M., & Colombo, R. (2023). Flow confinement effects on sUAS rotor noise. *Aerospace Science and Technology*, *143*, 108756.

Casalino, D., Romani, G., Zhang, R., & Chen, H. (2022). Lattice-boltzmann calculations of rotor aeroacoustics in transitional boundary layer regime. *Aerospace Science and Technology*, *130*, 107953.

Casalino, D., van der Velden, W. C., & Romani, G. (2019). Community noise of urban air transportation vehicles. In *Aiaa scitech 2019 forum* (p. 1834).

Drela, M., & Giles, M. B. (1987). Viscous-inviscid analysis of transonic and low reynolds number airfoils. *AIAA Journal*, *25*(10), 1347–1355.

Farassat, F., Dunn, M., & Spence, P. (1992). Advanced propeller noise prediction in the time domain. *AIAA journal*, *30*(9), 2337–2340.

Ghorbaniasl, G., Huang, Z., Siozos-Rousoulis, L., & Lacor, C. (2015). Analytical acoustic pressure gradient prediction for moving medium problems. *Proceedings of the Royal Society A: Mathematical, Physical and Engineering Sciences*, *471*(2184), 20150342.

Ghorbaniasl, G., & Lacor, C. (2012). A moving medium formulation for prediction of propeller noise at incidence. *Journal of Sound and Vibration*, *331*(1), 117–137.

Goyal, J., Sinnige, T., Ferreira, C. S., & Avallone, F. (2023, 6). Aerodynamics and far-field noise emissions of a propeller in positive and negative thrust regimes at non-zero angles of attack. American Institute of Aeronautics and Astronautics (AIAA). doi: 10.2514/6.2023-3217

Grande, E., Ragni, D., Avallone, F., & Casalino, D. (2022). Laminar separation bubble noise on a propeller operating at low reynolds numbers. *AIAA Journal*, *60*(9), 5324–5335.

Grande, E., Romani, G., Ragni, D., Avallone, F., & Casalino, D. (2022). Aeroacoustic investigation of a propeller operating at low reynolds numbers. *AIAA Journal*, *60*(2), 860–871.

Hanson, D. (1995). Sound from a propeller at angle of attack: a new theoretical viewpoint. *Proceedings of the Royal Society of London. Series A: Mathematical and Physical Sciences*, *449*(1936), 315–328.

Hanson, D. B. (1990). Noise radiation of propeller loading sources with angular inflow. In *13th aeroacoustics conference* (p. 3955).

Hanson, D. B., & Parzych, D. J. (1993). *Theory for noise of propellers in angular inflow with parametric studies and experimental verification* (Tech. Rep.).

Jamaluddin, N. S., Celik, A., Baskaran, K., Rezgui, D., & Azarpeyvand, M. (2024). Aerodynamic noise analysis of tilting rotor in edgewise flow conditions. *Journal of Sound and Vibration*, *582*, 118423.

Leng, Y., Jardin, T., Moschetta, J.-M., & Bronz, M. (2021). Analytic model of proprotor forces and moments at high incidence. *Journal of the American Helicopter Society*, *66*(4), 1–15.

Magliozzi, B., Hanson, D., & Amiet, R. (1991). Propeller and propfan noise. *Aeroacoustics of flight vehicles: theory and practice*, *1*, 1–64.

Pereira, L. T. L., Ragni, D., Romani, G., & Casalino, D. (n.d.). Accuracy of tonal noise prediction of propellers via numerical simulations and experimental campaigns. In *30th aiaa/ceas aeroacoustics conference (2024).* doi: 10.2514/6.2024-3267

Pii, L. M., Casalino, D., Romani, G., & Singal, K. (2024). Aeroacoustic optimization of an axial cooling fan with fundamental observations. In *30th aiaa/ceas aeroacoustics conference.* doi: 10.2514/6.2024-3268

Roger, M., & Moreau, S. (2005). Bach-scattering correction and further extensions of amiet's trailing edge noise model, part 1: Theory. *Journal of Sound and Vibration*, *286*(3), 477–506.

Romani, G., Grande, E., Avallone, F., Ragni, D., & Casalino, D. (2022a). Computational study of flow incidence effects on the aeroacoustics of low blade-tip mach number propellers. *Aerospace Science and Technology*, *120*, 107275.

Romani, G., Grande, E., Avallone, F., Ragni, D., & Casalino, D. (2022b). Performance and noise prediction of low-reynolds number propellers using the lattice-boltzmann method. *Aerospace Science and Technology*, *125*, 107086.

Schlinker, R. H., & Amiet, R. K. (1981). Helicopter trailing edge noise. *NASA CR-3470*.

Yunus, F., Grande, E., Casalino, D., Avallone, F., & Ragni, D. (2022). Efficient low-fidelity

aeroacoustic permanence calculation of propellers. *Aerospace Science and Technology*, *123*, 107438.

Yunus, F., von den Hoff, B., & Snellen, M. (2024). Predicting tonal noise of full-electric propeller-driven aircraft in outdoor environments using low-order models. In *30th aiaa/ceas aeroacoustics conference (2024)* (p. 3418).